A molecular dynamics investigation of laminar pyrocarbons elasticity up to high-temperatures

Franck Polewczyk, Paul Lafourcade, Nicolas Pineau, Christophe Denoual, Gérard Vignoles, Jean-Marc Leyssale

A molecular dynamics investigation of laminar pyrocarbons elasticity up to high-temperatures

Franck Polewczyk[a,b,c], Paul Lafourcade[a,b,*], Nicolas Pineau[a,b], Christophe Denoual[a,b], Gérard L. Vignoles[d], Jean-Marc Leyssale[c,*]

[a] *CEA DAM DIF, 91297 Arpajon, France*
[b] *University of Paris-Saclay, LMCE, 91680 Bruyères-le-Châtel, France*
[c] *University of Bordeaux, CNRS, Bordeaux INP, ISM, UMR 5255, F-33400 Talence, France*
[d] *University of Bordeaux, CNRS, CEA, Safran: LCTS (UMR5801), F-33600 Pessac, France*

Abstract

The mechanical properties of anisotropic carbons such as the pyrocarbon (pyC) matrices in C/C composites remain poorly documented, especially at elevated temperatures where these materials find most of their applications. We provide here a comprehensive molecular dynamics investigation of the high temperature – up to 4000 K – elastic behavior of six nanoscale pyC models in the context of fast temperature increases, not allowing for major structural modifications such as graphitization. We show that the structure of the most anisotropic and less disordered carbons, like the rough laminar (RL) pyC, is mostly not affected by annealing at the nanocecond timescale, aside from healing unstable defects like two-coordinated atoms at graphene edges. Conversely, highly disordered and less anisotropic carbons like the smooth laminar (SL) pyC show some significant rearrangements at grain boundaries and the development of some limited microporosity. The elastic constants of all highly anisotropic models moderately decrease with increasing temperature, somehow similarly to what is observed for graphite. Elastic constants of the SL pyC show a stronger decrease at high temperature, due to the decrease in density even though all models retain an important degree of stiffness up to 4000 K.

In the realms of aerospace and nuclear energy, low-temperature pyrolytic carbons (pyCs), deposited through chemical vapor deposition (CVD) or infiltration (CVI) techniques on surfaces or within porous materials, play a pivotal role [1, 2]. Combining low weight, exceptional mechanical and thermal properties as well as high melting points and low porosity, these materials are primarily used as constituents in continuous-fiber reinforced composites, either as thick matrices in carbon/cabon (C/C) composites [3, 4], or as thin interphases in ceramic matrix composites (CMCs)[5].

Applications of CMCs with pyC interphases are mostly found as structural parts of devices in aeronautics and nuclear industries [5, 6, 7], involving mild to elevated temperatures. C/C composites also act as structural elements of space rocket motors [8] and brakes in aeronautical and terrestrial transportation[9, 10]. The exceptionally high melting point of carbon combined to a very low coefficient of thermal expansion also allows C/C composites to be a material of choice when extremely high temperatures and heat fluxes are encountered. A particularly noticeable application of C/C composites is as thermal protection systems [11], especially within the development of hypersonic projectiles[12, 13].

Critical to the design of C/C composites is the control of their mechanical and thermal properties, and a well-informed design should include knowledge of the elastic tensors, thermal expansion coefficients and thermal conductivity of all the constituents in the whole temperature range relevant to the applications. To date, this knowledge clearly does not exist for the pyC matrices. Focusing on the elastic behavior, only two reports of the complete elastic tensors, under the form of Young moduli and Poisson coefficients and based on tensile/compression [14] and ultrasonic [15] measurements at room temperature, are available to our knowledge. The longitudinal moduli (*i.e.* parallel to the main direction of graphene alignment) measured on these pyC monoliths, are lower by about an order of magnitude with respect to those measured by Sauder *et al.* based on tensile tests on microcomposites [16], indicating the difficulty in obtaining reliable data for this type of materials. Furthermore, the work of Sauder *et al.* remains to our knowledge the only report on pyC elastic properties at elevated temperatures (up to $\sim$ 2500 K), although only the longitudinal modulus was measured. Furthermore, investigating carbon structure and mechanical properties under high temperature at short (nanosecond) timescales is crucial for ensuring the reliability and performance of composite materials in spatial and defense applications, where they are often subjected to extreme thermal stresses involving fast processes. Under-

*Corresponding author
Email addresses: paul.lafourcade@cea.fr (Paul Lafourcade), jean-marc.leyssale@u-bordeaux.fr (Jean-Marc Leyssale)

standing these properties at such timescales helps in designing materials that can withstand sudden thermal shocks and maintain structural integrity in critical mission environments.

PyC matrices exhibit a wide variety of textures, depending on the gas phase precursor and deposition/infiltration conditions [17, 18, 19]. Historically, pyC textures were first classified according to polarized light optical microscopy (PLOM)[20], characterizing their anisotropy at the scale of the entire fiber coatings (*i.e.* μm scale). The high anisotropy rough laminar (RL), low anisotropy smooth laminar (SL), and isotropic (ISO) textures [21, 20], as well as the dark laminar (DL) texture [22], intermediate between ISO and SL, were identified. Later on, pyC matrices were also extensively investigated using High-Resolution Transmission Electron Microscopy (HRTEM) and Bourrat *et al.* introduced the orientation angle (OA), derived from intensity profiles along the 002 arcs in Selected Area Electron Diffraction (SAED) patterns, as a sub-micrometer evaluation of texture anisotropy [23]. Reznik and Hüttinger[24] expanded on this, proposing a classification of pyC nanotextures based on OA values: Isotropic (ISO) when OA $\sim 180°$; pyCs with OA = 180°, low texture (LT) when $180° > \text{OA} \geq 80°$, medium texture (MT) when $80° > \text{OA} \geq 50°$ and high texture (HT) when OA $< 50°$. According to this classification, the long-known rough laminar (RL) and smooth laminar (SL) pyrocarbons belong to the HT and MT categories, respectively.

Aside from texture, describing the distribution of 002 directions in the material, the nanostructure of pyCs is best described by the analysis of X-ray or neutron diffraction patterns. As prepared, the nanoscale order of these materials, with turbostratic stacking of graphene layers (*i.e.* without in-plane orientational order), is characterized by the unique presence of 00*l* (out-of-plane) 3D features and 2D *hk* asymmetric (in-plane) bands. The out-of-plane L_c and in-plane L_a coherence lengths extracted from the latter, characterizing the extent of "crystalline" domains in the materials, are typically of 2 to 5 nm, in both directions, for as-prepared pyCs [25, 26]. It is worth mentioning that these lengths can significantly increase upon high-temperature annealing for high-texture pyCs, which can even develop some 3D crystallinity. Those pyCs therefore belongs to graphitizing carbons. Conversely, the structure improvement of medium and low texture pyCs remains limited, without 3D crystallinity whatever the annealing temperature, and these carbons are defined as "non graphitizing".

The work presented here is part of a long-standing research effort aiming at producing a bottom-up multi-scale structure/elasticity relationship for pyC matrices, starting from the nanoscale [27, 26, 28, 29, 30, 31, 32, 33]. Especially, in a very recent work, Polewczyk *et al.* have proposed a poly-granular atomistic reconstruction (PG-IGAR) method, to produce a large database of models of textured carbons, covering both MT and HT pyC domains and spanning wide and uncorrelated ranges of L_a, L_c and OA values 32. A recent publication describes the detailed relationship, derived from a machine learning analysis, between the different structural and textural parameters and the complete, room temperature, elastic tensors [33]. Although significantly different from experimental measurements, as larger-scale textural effects are neglected, the obtained room temperature elastic model can be inserted in a continuum mechanics mesoscale model of the texture. In the same spirit we present here a detailed investigation of the evolution of the elastic tensor of six atomistic models, identified as models of actual pyC materials, at temperatures ranging from 300 to 4000 K, and compare the elastic behavior of the pyC models to the one reported recently for crystalline graphite[34].

1. Models and methods

1.1. Atomistic models of pyCs

We consider here six atomistic models of the database from Polewczyk *et al.* [32] that were previously identified as best reproducing the structural/textural parameters of six well-characterized isolated pyC samples [25, 26]. These models include an RL pyC, an SL pyC, and a regenerative laminar (ReL) pyC[35] – another HT pyC, more defective than RL – as prepared and after heat treatments at 1300, 1500 and 1700°C. All the models contain 206950 atoms enclosed in nearly cubic periodic cells of $\sim$ 12.4 nm side lengths. Their main structural/textural parameters are summarized in table 1. One observes that all models show few-nm large coherent domains with interlayer spacings typical of turbostratic carbons, namely about 0.01 nm larger than in AB stacked layers (*i.e* 0.335 nm in Bernal graphite). They are all rather dense, therefore showing no microporosity, and, as expected, with OAs lower than 50°, all but the SL model, belong to the HT pyC category, the latter being in the MT category. We also observe that most parameters are extremely close to experimental data aside from two exceptions: the ReL_{1700} model has a significantly underestimated L_c value, as the experimental one is actually larger than the whole simulation cell, and the SL model is slightly too dense, indicating that the actual experimental sample certainly contains some porosity.

Snapshots of the models are presented in Figure 1 where atoms are colored according to their local atomic environments. Following Farbos *et al.* [36] and Vukovic *et al.* [37], atoms with one, two, three and four neighbors are noted as C_1, C_2, C_3 and C_4, respectively; and the C_3 (sp^2) atoms are subdivided into four categories, which are, by order of priority: C_3^α corresponding to atoms in three hexagons, C_3^β corresponding to atoms involved in at least one non-hexagonal ring, C_3^γ corresponding to atoms bonded to a C_4 atom and C_3^δ corresponding to atoms bonded to a C_2. Qualitatively speaking, one observes that, in agreement with the data in

Table 1: Structural/textural parameters of the PG-IGAR pyC models at 300 K and 1 atm from Polewczyk et al. [32]. In parentheses, the experimental data from Weisbecker et al. [25] and Farbos et al. [26] are given for comparison.

pyC	L_c (nm)	L_a (nm)	OA (deg.)	d_{002} (nm)	ρ (g/cm^3)
SL	2.3(2.6)	3.3(3.3)	67(68)	0.342(0.345)	2.17(1.93)
RL	5.5(5.2)	4.6(4.6)	29(22)	0.346(0.345)	2.18(2.12)
ReL	2.9(2.9)	2.3(2.6)	36(40)	0.347(0.346)	2.13(2.11)
ReL_{1300}	3.9(3.8)	3.3(3.1)	37(43)	0.349(0.347)	2.15(2.16)
ReL_{1500}	6.1(6.3)	4.1(4.1)	32(30)	0.346(0.345)	2.18(2.18)
ReL_{1700}	7.6(13.3)	5.2(6.2)	27(27)	0.345(0.343)	2.19(2.18)

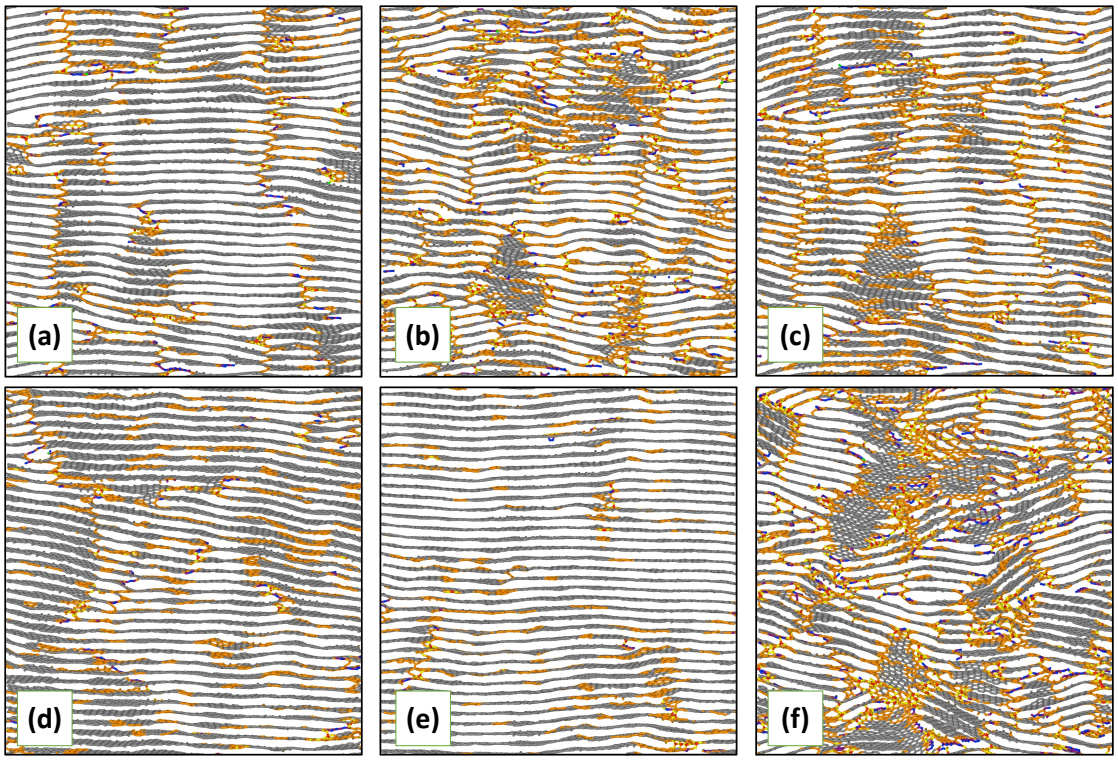

Figure 1: 1 nm-thick cross-sections of (a) RL, (b) ReL, (c) ReL_{1300}, (d) ReL_{1500}, (e) ReL_{1700} and (f) SL models at room temperature. Colors assigned to atoms correspond to different local atomic environments: C_1 (green), C_2 (blue), C_3^{α} (gray), C_3^{β} (orange), C_3^{γ} (yellow), C_3^{δ} (purple) and C_4 (red). Horizontal and vertical cell lengths are all of about 12.4 nm.

table 1, the ReL_{1700} and RL pyC models are those with the largest coherent domains (formed by C_3^α atoms) and highest degrees of anisotropy, while the SL pyC model has the smallest domains (with the ReL pyC model) and lowest textural anisotropy. Defects, and especially C_2, C_4, C_3^γ and C_3^δ atoms, are mostly located at domain boundaries. The latter form many types of defects including point defects, edge dislocations, extended screw dislocations, etc. as reported in many recent investigations [27, 26, 38, 39]. Graphene layers are either interconnected to neighboring domains in the *c*-axis direction via a disordered network of screw dislocations – the so-called "car park access ramp" [27] – where most C_4 atoms reside, or in the *a*-axis direction by grain boundaries made by networks of pentagon/heptagon pairs. The snapshots also visually agree with the diffraction data in showing that the ReL_{1700} pyC model is the most ordered one with the largest coherent domains, both in-plane and out-of-plane, and the largest anisotropy, while the SL pyC has the smallest domains and anisotropy. Atomistic configurations of the six models relaxed at 300 K and 1 atm are given in `.xyz` format in the supplementary material.

Table 2: Room temperature isothermal elastic constants in GPa of the six pyC models (data from Polewczyk *et al.* [33]). A_u is the universal anisotropy index[40].

pyC	C_{11}	C_{33}	C_{12}	C_{13}	C_{44}	C_{66}	A_u
SL	427	26.8	61.3	32.9	22.5	147	13.9
RL	687	11.6	86.3	14.1	3.3	191	101
ReL	564	13.0	67.8	20.0	6.9	160	49.6
ReL_{1300}	600	12.8	68.1	16.2	7.2	152	49.6
ReL_{1500}	586	12.6	93.3	16.9	4.7	159	64.5
ReL_{1700}	703	9.3	79.7	10.9	1.1	165	263

The room temperature isothermal (*i.e.* quasi-static) elastic constants of the six pyC models, computed by Polewczyk *et al.* [33], are given in table 2. The universal anisotropy index A_u [40] defined as

$$A_u = 5\frac{G^V}{G^R} + \frac{K^V}{K^R} - 6 \quad (1)$$

where G and K indicate estimates of the shear and bulk moduli, respectively, according to the Voigt (V superscript) and Reuss (R superscript) models, quantifies the elastic anisotropy of a material. The determination of K^V, K^R, G^V and G^R from the elastic tensors is described in previous work[34, 33]. This indicator allows for an easier comparison of the models. As expected the medium texture SL pyC model is the one with lowest mechanical anisotropy. Regarding the ReL pyC models, one observes that elastic anisotropy builds up with the heat treatment temperature such that the RL pyC model falls in between the ReL pyC models heat treated at 1500 and 1700°C, respectively, which is compatible with the similar L_a, L_c and OA values obtained for these models (see table 1). It is worth recalling that, as demonstrated in Ref. 33, the elastic constants presented in table 2 do not allow reproducing some experimental data. For instance, the longitudinal (in-plane) Young's moduli derived from the elastic tensors were shown to overestimate the results of tensile tests on single pyC-coated fibers [16] by factors of 2 to 6. As discussed in Ref. 33, the difference most certainly arises from the size of the models (12.4 nm), which cannot capture texture at the deposit scale.

1.2. Molecular dynamics simulations

Molecular dynamics (MD) simulations were performed with the `STAMP` [41] (Simulations Temporelles Atomistiques Massivement Parallélisées) code with interactions between C atoms described by the LCBOPII potential [42] and periodic boundary conditions in the three cartesian directions. MD trajectories under both canonical (NVT) and isothermal-isobaric (NPT) conditions were integrated using a velocity-Verlet integrator [43] operating with a 0.25 fs timestep. Temperature (both NVT and NPT) and pressure (NPT only) were controlled by Nosé-Hoover-Andersen thermostat and barostat operating with damping constants of 0.1 and 1.0 ps, respectively.

First, all the models were subjected to short heat treatments at different temperatures, from 500 to 4000 K by step of 500 K, in order to anneal the weakest defects prior to mechanical testing. For this, new sets of velocities, drawn from Maxwell-Boltzmann distributions at the suited temperatures, were attributed to the configurations previously equilibrated at 300 K and 1 ns long NPT MD simulations were performed to equilibrate the pyC models at the different temperatures. The hydrostatic pressure was set to 1 atm. Equilibrium properties were computed from the last 100 ps of MD. The final configurations of these simulations then served as initial configurations for the NVT MD simulations aimed at computing elastic constants. In addition, the exact same procedure was used to bring these annealed configurations back to 300 K, in order to quantify the change in structure and properties induced by these short annealing simulations.

1.3. Calculation of the elastic constants

Isothermal elastic tensors were computed in the exact same way as in the recent publication by Polewczyk *et al.* [33]. It is based on the calculation of stress-strain relationships obtained from series of well-equilibrated MD simulations at small uniaxial tensile and shear strains. As in Ref. 33, the considered strain ranges are 1 to 3 % for tensile deformations and -1 to 1 % for shear deformations, with, in both cases, a 0.1 % increment.

Following the application of strain, the simulation cell underwent equilibration in the NVT ensemble for a duration of 100 ps to allow for stress relaxation via the reorganization of atomic coordinates. The stress tensor was then obtained by averaging stress components over the last 20 ps of the

trajectories. Then, elastic constants were determined by performing linear fits of the stress *vs.* strain curves. As in former work [34], C_{11} and C_{12} were averaged from tensile tests performed in the x and y directions, C_{33} was obtained from tensile tests in the z direction, C_{13} was averaged from tensile tests performed in the x, y and z directions (2 independent evaluations along the z axis), C_{44} was averaged from shear tests in the xz and yz planes and C_{66} was explicitly calculated from shear tests in the xy plane.

1.4. Nanostructure and nanotexture analysis

As in former studies [26, 36, 37, 32], single configuration analysis was performed to determine *i*) the coordination of individual atoms, using a 1.85 Å cutoff distance, and *ii*) the list of shortest path rings (SPR)[44] present in the system. This allows us to classify the atoms according to their local environments as discussed above (C_2, C_3^{α}, C_3^{β}, etc.).

As in Ref. 32, the structural parameters L_c and L_a were extracted from the structure factors $S(Q)$ obtained from the real-space pair distribution function $G(r)$ averaged over the MD trajectory at equilibrium:

$$S(Q) = 1 + \frac{1}{Q}\int_0^{r_{max}} G(r)\sin(Qr)dr \qquad (2)$$

where r is the interatomic distance and r_{max} was set to 6 nm (*i.e.* $\sim$ half the simulation cell width). Structure factors was converted from Q space to 2θ space according to the relation $Q = \frac{4\pi\sin(\theta)}{\lambda}$ where $\lambda = 1.542$ Å was taken as the X-Ray Cu K_α wavelength. As in former works [25, 26, 32], the 002 peak was fitted with a pseudo-Voigt function and the 2θ domain corresponding to the 10 band and 004 peak was adjusted with the sum of a skewed Gaussian (10) and a Pearson VII function (004). The d_{002} parameter was obtained from the 002 peak position using Bragg's law. The Scherrer-Warren relations – $L_{a,c} = K_{a,c}\lambda/(\beta cos(\theta))$ where $K_a = 1.77$, $K_c = 1$, β is the full width at half maximum (FWHM) of the peak and θ is the diffraction half-angle – were used to determine L_a and L_c from the fitted 10 and 002 features, respectively.

HRTEM image simulation was performed on single configurations using `Dr Probe` [45]. Standard microscope parameters were used [25, 26]: 300 kV voltage, 1.2 and 1.5 mm spherical and chromatic aberration, respectively, -58 nm Scherzer defocus and 7 *mm* defocus. From the latter an SAED pattern is obtained by fast Fourier transform (FFT), from which an intensity profile is gathered along the 002 arcs. OA is determined as the FWHM of this profile using a gaussian fit. The full procedure is described in Ref. 32.

2. Results

2.1. Effect of annealing on room temperature properties

Figure 2 shows the effect of the short thermal annealing treatment on some important structural, textural and thermodynamic properties at room temperature. Overall we observe that the properties of the three less disordered models, namely the RL, ReL_{1700} and ReL_{1500} pyC models (*i.e.* those having the largest L_a and L_c, and lowest OA and enthalpy), are almost unaffected by the annealing scheme. The small fluctuations observed for these models are certainly within the error bars associated to the calculation of the properties, even though such errors were not explicitly computed.

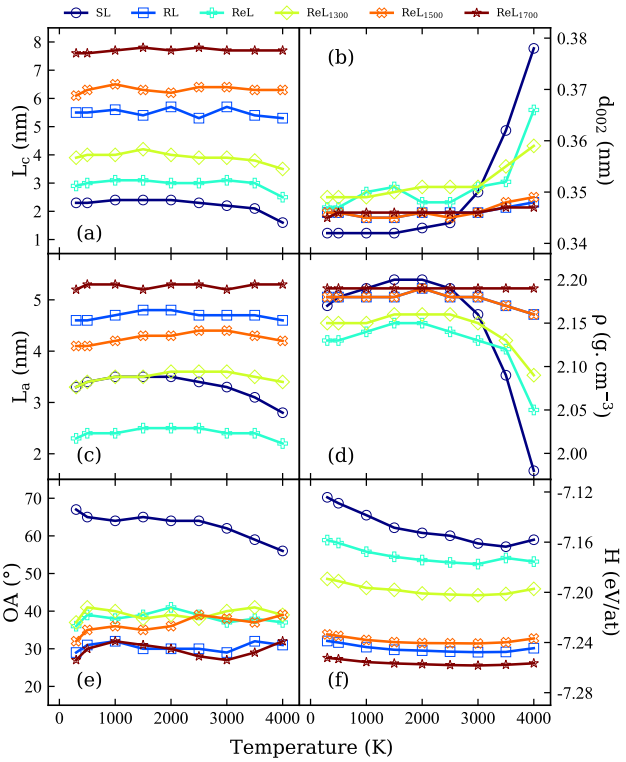

Figure 2: Evolution of various structural, textural and thermodynamic properties with temperature after 1 ns-long annealing simulations: (a) L_c, (b) d_{002}, (c) L_a, (d) ρ, (e) OA and (f) enthalpy H.

Conversely, the properties of the three most disordered models – SL, ReL and ReL_{1300} – show some dependence on the annealing temperature. A decrease in L_c (Fig. 2(a)) is clearly observed for these models around 4000 K and a similar behavior is observed for L_a (Fig. 2(c)), with data seeming to pass through a maximum for annealing temperatures around 2000-2500 K, before falling slightly below the 300 K values at higher annealing temperatures. However, the evolution of values also remains close to the error associated to the extraction of L_a and L_c from the structure factors given in Fig. S1. The interlayer spacing d_{002} unambiguously increases with annealing temperature above 2000-3000 K for the ReL, ReL_{1300} and SL pyC models (Fig. 2(b)), while density decreases (Fig. 2(d). These parameter evolutions are particularly significant for the SL pyC model for which d_{002} and ρ reach values of 0.378 nm and 1.98 g/cm^3, respectively, after annealing at 4000 K.

The orientation angle OA (Fig. 2(e)) of the ReL_{1500} pyC

model slightly increases from $\sim 30°$ at 300 K to $\sim 40°$ at 4000 K, indicating a slight decrease in texture anisotropy for this model. Conversely, OA decreases by more than 10° for the SL pyC model, indicating an increase in texture anisotropy. No significant change in OA is observed for the four other pyC models. These observations correlate fairly well with the evolution of the HRTEM images after annealing at 4000 K, presented in Fig. S2 and Fig. S3. Finally, we see in Fig. 2(f) that these observed evolutions in the structure and texture parameters of the SL, ReL and ReL_{1300} models induce a decrease in the models' atomic enthalpy, and hence a stabilization of the latter, the enthalpies of the three most ordered models being almost unchanged by annealing.

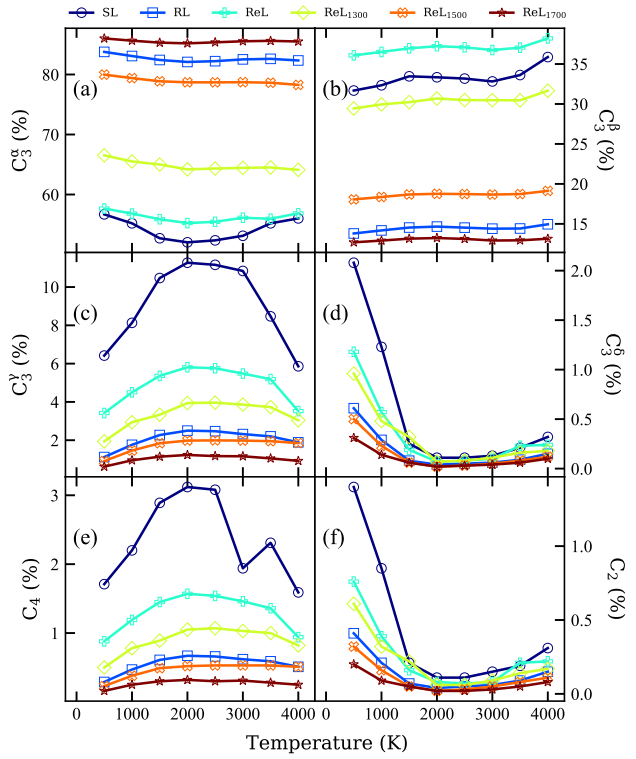

Figure 3: Evolution of the proportions of different atom types with heat treatment temperature. (a): C_3^α, (b): C_3^β, (c): C_3^γ, (d): C_3^δ, (e): C_4 and (f) : C_2.

Fig. 3 presents the evolution of the distributions of the different atomic environments with annealing temperature and helps identifying the key changes in local structure due to annealing. The most affected types of atomic environments are the C_2 atoms and hence the C_3^δ (C_3 bound to C_2), as well as the C_4 and hence the C_3^γ (C_3 bound to C_4). The C_2 (Fig. 3(f)) and C_3^δ (Fig. 3(d)) atoms, present up to 2% for the SL pyC model before annealing, almost disappear after annealing at $\sim$ 2000 K. Their proportions increase slightly after annealing to higher temperatures, yet remaining well below 0.5 %, and at considerably lower values than prior to annealing. The proportions of C_4 (Fig. 3(e)) and C_3^γ (Fig. 3(c)) atoms also show a non monotonic evolution with annealing temperature, this time passing through a maximum at about 2000 K. Again, the most affected models are the most disordered ones – SL, then ReL and then ReL_{1300} by order of importance – which were already counting the largest amounts of these atom types prior to annealing. The proportions of atoms in graphene-like environments (C_3^α) show very slight decreases with annealing temperature (Fig. 3(a)) while the proportions of C_3^β atoms, typical of defects of graphenic grain boundaries, show very slight increases (Fig. 3(b)) for the most ordered models (RL, ReL_{1500} and ReL_{1700}). This trend is stronger for the most disordered models which is consistent with the slight reductions in L_a observed in Fig. 2(c). Finally, it is interesting to note that the average number of rings per atom (Fig. S4) remains relatively constant and close to the value for crystalline graphene and graphite (0.5) for the three less disordered models, with values in the 0.48-0.50 range. This number is lower and evolves more with annealing temperature for the three other models. Especially for the SL pyC, the average number of rings per atom, initially of $\sim$ 0.415, decreases to $\sim$ 0.395 after annealing at 2000 K, and increases back to $\sim$ 0.44 after annealing at 4000 K.

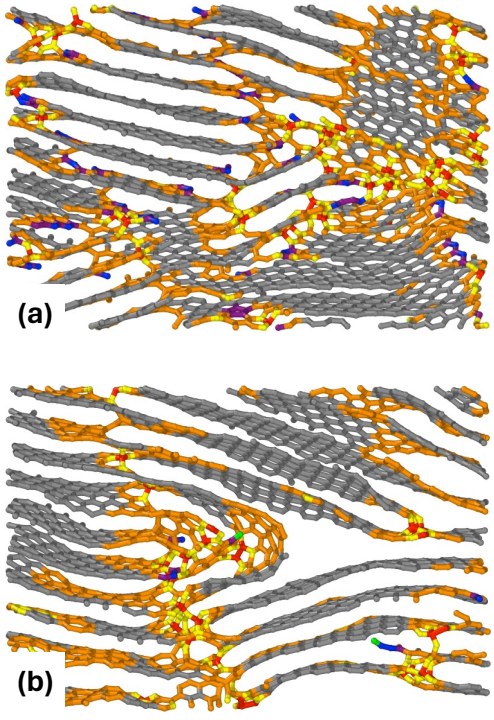

Figure 4: Snapshots of one nm-thick cross-sections of (a) SL before heat treatment and (b) SL treated at 4000 K. Colors assigned to atoms correspond to : C_1 (green), C_2 (blue), C_3^α (gray), C_3^β (orange), C_3^γ (yellow), C_3^δ (purple) and C_4 (red). Horizontal and vertical cell lengths have dimensions of 6.0 × 1.0 × 4.0 nm. Panels (a) and (b) do not necessarily correspond to the same location in the models.

The equivalent of Fig. 1 for the models annealed at 4000 K and cooled down to room temperature is provided in Fig. S5. Although some differences can be observed on the local

structure, the overall nanotexture of the five HT models is almost unaffected by the 4000 K annealing simulation. However, comparing the snapshots in Fig. 1(f) and Fig. S5(f), one observes significant modifications of the nanostructure of the SL model after annealing at 4000K. In addition to the increase in anisotropy measured by the decrease in OA, we observe a significant smoothing of the structure. Indeed, the sharp boundaries between misoriented/tilted grains observed at 300 K (Fig. 1(a)) are replaced by much smoother curved graphene layers like the double folded layers visible in the middle-left area of Fig. 1(b), reminiscent of the grafold [46] or collapsed nanotube [47] structures. This folded structure, minimizing edge energy, acts like a high angle edge dislocation, creating a visible micropore in its vicinity (on its right), which agrees well with the decrease in density. Also worth mentioning is the formation of a more traditional prismatic edge dislocation [48] in the middle-right side where two layers merge into a unique one.

Overall, while long timescale high temperature treatments are generally expected to increase the coherence lengths, decrease the interlayer distance and increase the anisotropy of graphitizable carbons, we observe here that at the nanosecond timescale, such treatments only result in the annealing of weakest local defects, without significant evolution in structure and texture.

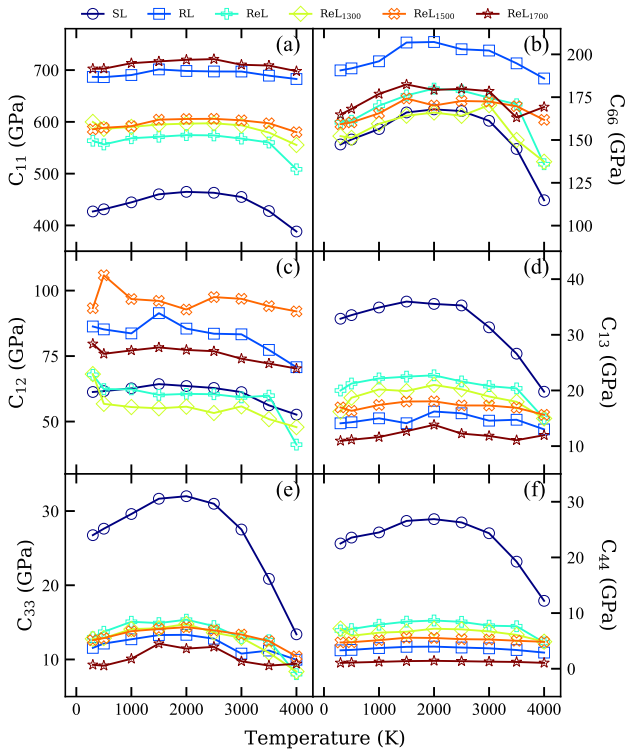

Figure 5: Evolution of the room temperature elastic constants with annealing temperature: (a) C_{11}, (b) C_{66}, (c) C_{12}, (d) C_{13}, (e) C_{33} and (f) C_{44}.

Figure 5 presents the evolution of the room temperature elastic constants due to annealing. As expected from the previous discussions, the elastic constants of the most ordered pyC models do not significantly change with annealing temperature, even though some constants seems to show a slight bell-shape evolution with maximum values for annealing temperatures around 2000 K. This is evident for the SL pyC model for which all constants increase up to $\sim$ 2000 K, then decrease significantly when increasing further the annealing temperature. The evolution of the elastic constants actually correlates very well with the changes in density observed in Fig. 2(d), which, we assume, is the most significant factor for the evolution of the room temperature elastic tensors.

2.2. High temperature properties

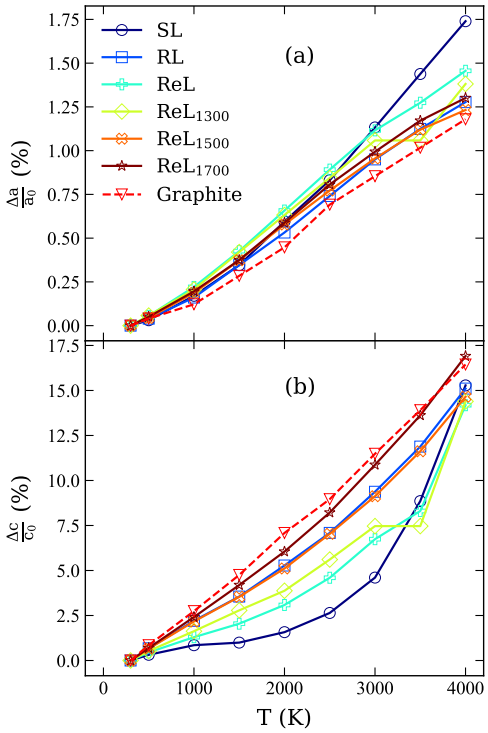

Figure 6: (a) Longitudinal and (b) transverse dimensional change with increasing temperature of the pyC models and graphite. Parameters a and c correspond respectively to the simulation cell lengths in the longitudinal and transverse directions, respectively. a_0 and c_0 are reference values taken at 300 K.

The evolution of longitudinal (a-axis) and transverse (c-axis) cell dimensions with temperature is shown in Figure 6, the equivalent properties computed for crystalline graphite[34] are given for comparison. As discussed in Ref. 34, we recall here that MD calculations of thermal expansion is only semi-quantitative below the Debye temperature ($\sim$ 2000 K[49]) where zero-point energy effects have a dominant effect on these properties, especially in the longitudinal direction [50, 51]. Nevertheless, comparing the results obtained for the pyC models to those obtained earlier for graphite, we observe that, as expected, thermal expansion is more pronounced in the longitudinal direction than in the

transverse direction, and that the pyC models tends towards the values for graphite with increasing structural and textural quality (*i.e.* increasing coherence lengths and decreasing OA). One can notice that, despite rather small coherence lengths ($\sim$ 5 nm), the most ordered and anisotropic pyC models (RL, ReL_{1500} and ReL_{1700}) show very similar thermal expansion to the almost linear curves obtained for graphite. The three other models are a bit further away, especially for the transverse data at low temperatures for the SL pyC model. This is expected for the latter material which is far less anisotropic than the others. However the thermal expansion of this model significantly increases with increasing temperature above 2500 K, which is concomitant to the significant decrease in the OA parameter experienced by this model at these temperatures.

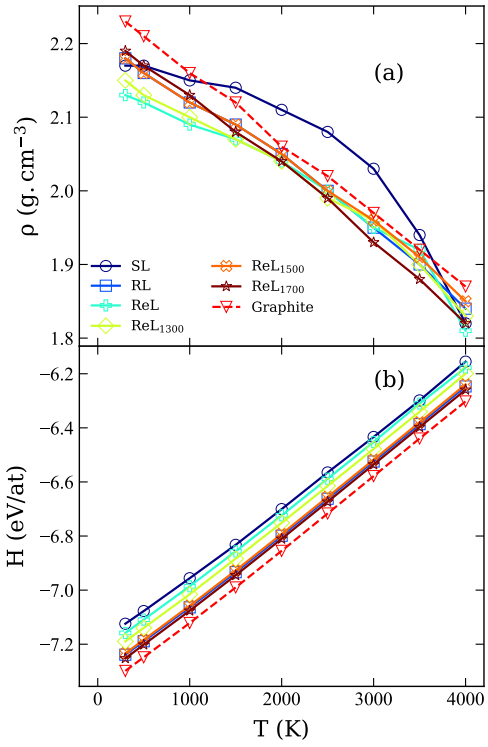

Figure 7: Evolution with temperature of (a) density and (b) enthalpy.

Figure 7 shows the evolution of density ρ and enthalpy H of the pyC models and graphite with temperature. Pretty similar comments to those made for the c-axis expansion can be made for the density (Fig. 7(a)). An almost linear decrease of ρ with temperature is indeed observed for the most ordered and anisotropic pyC models, very close, albeit with slightly lower values, to the linear trend obtained for graphite. Density also decreases with temperature for the three other models, yet in a much less linear fashion, especially for the SL pyC model. Enthalpy increases linearly with T for all models with graphite and the SL pyC showing the lowest and largest values, respectively (Fig. 7(b)). This means that structural changes in terms of bond properties are not very significant, in agreement with the changes in atomic environment statistics presented in Fig. 3.

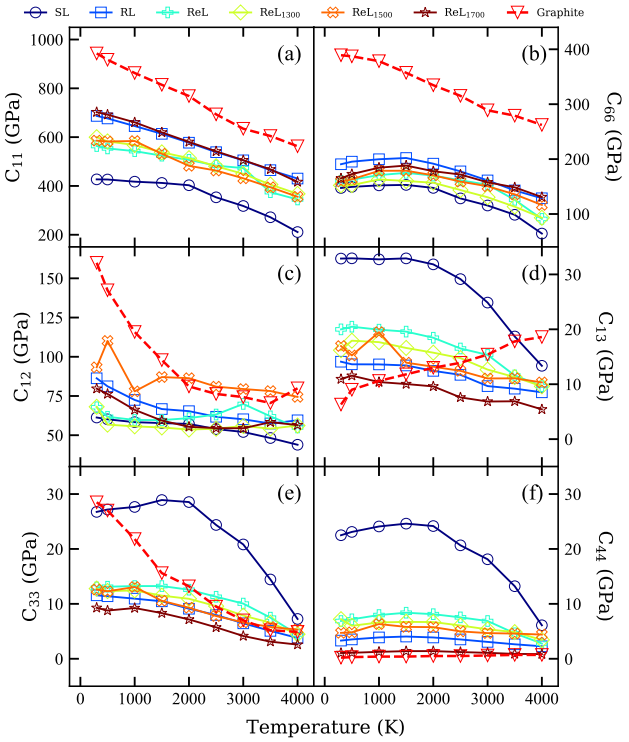

Figure 8: Evolution with temperature of the elastic constants of the six pyC models and graphite: (a) C_{11}, (b) C_{66}, (c) C_{12}, (d) C_{13}, (e) C_{33} and (f) C_{44}.

The evolution of the elastic constants with temperature is presented in Figure 8. Numerical values of all the constants are given in table S1-S7. Overall we observe that the elastic constants of the pyC models evolve with temperature in a very similar way and magnitude to those of graphite. The hierarchy of models in terms of C_{ij} values is overall respected, regardless of temperature. Furthermore, the somehow anomalous increase of C_{13} with temperature observed for graphite is not observed for the pyC models. Unsurprisingly, the SL pyC model is the one with the lowest purely longitudinal elastic constants (C_{11}, C_{12} and C_{66}, and the largest constants involving the transverse direction (C_{33}, C_{13} and C_{44}). We also observe a significant decrease in the SL pyC's elastic constants, especially the transverse ones, when temperature exceeds 2500 K, which can be explained by the significant decrease in density and increase in d_{002} observed for this model above this temperature.

Fig. 9 shows the evolution with temperature of the universal anisotropy index A_u for the six pyC models and graphite. While the values for graphite strongly decreases with T, by about an order of magnitude from 300 to 4000 K, A_u for the pyC models remain fairly constant for most models and temperatures. The only significant change for A_u is observed for the SL pyC model above 3000 K, which is consistent with the significant decrease in OA observed for this model at those temperatures (see Fig. 2(e)). Also, it is interesting

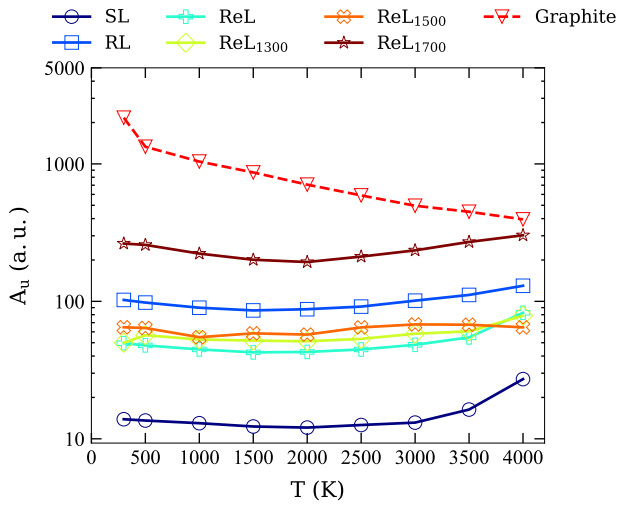

Figure 9: Universal anisotropy index as a function of temperature for the six pyC models. Data for graphite are taken from reference [34].

to note that at 4000 K the most ordered model, the ReL_{1700} pyC model, has a similar anisotropy index to graphite.

3. Conclusion

In this work we have presented the first molecular dynamics investigation of the elastic behavior of pyC matrices subjected to a rapid increase in temperature. Six pyC models of various textures, including five HT pyCs, the as-prepared RL and ReL pyCs as well as ReL pyCs heat treated at 1300, 1500 and 1700°C, and one MT pyC, the as-prepared SL pyC. We started by investigating the effect of 1 ns long annealing at the various temperatures on the structure/texture of the pyC models and observed a very limited effect, even at the highest temperature (4000 K), on the most anisotropic and less disordered models, namely the RL pyC and the ReL pyC heat treated at 1500 and 1700°C. Conversely, the SL pyC (MT) was shown to undergo significant rearrangements at domain boundaries, leading to the formation of graphene loops and to the apparition of small micropores. Regarding the bonding structure, annealing mostly results into the disappearance of unsaturated (C_2) atoms.

With increasing temperature, all the elastic constants of the HT pyC models decrease smoothly, and to a limited extent – typically less than 50%. The decrease in the elastic constant of the SL pyC (MT) is more abrupt above 2000 K, which can be related to the strong decrease in density observed at these temperatures. Overall, all the pyCs retain high stiffness, even at the largest T investigated (4000 K), for such rapid solicitations (1 ns).

Interestingly, while the mechanical anisotropy – computed via the universal anisotropy index A_u – of graphite has been shown to decrease significantly with increasing T, A_u remains fairly constant for the HT pyCs, whatever the temperature, and even increases with T (for T 3000 K) for the SL pyC due to an increase in the texture anisotropy of this model at these temperatures. Eventually, at 4000 K, the A_u index of the most ordered pyC model is relatively close to the one of graphite.

CRediT authorship contribution statement

Franck Polewczyk: Methodology, Software, Formal analysis, Investigation, Visualization, Data curation, Writing – original draft. **Paul Lafourcade**: Conceptualization, Methodology, Software, Formal analysis, Resources, Data curation, Writing – original draft. **Nicolas Pineau**: Conceptualization, Software, Resources, Writing – review & editing. **Christophe Denoual**: Conceptualization, Software, Resources, Writing – review & editing. **Gérard Vignoles**: Conceptualization, Resources, Writing – review & editing. **Jean-Marc Leyssale**: Conceptualization, Methodology, Software, Formal analysis, Resources, Data curation, Writing – original draft.

Declaration of competing interest

The authors declare that they have no known competing financial interests or personal relationships that could have appeared to influence the work reported in this paper.

Acknowledgments

Financial support from the French Ministry of Defence - Defence Innovation Agency is gratefully acknowledged by FP. Atomistic simulations were performed using the computational resources of the CEA/DAM.

References

[1] A. Oberlin, Pyrocarbons, Carbon 40 (2002) 7–24. doi:10.1016/S0008-6223(01)00138-5.

[2] P. Delhaès, Chemical vapor deposition and infiltration processes of carbon materials, Carbon 40 (5) (2002) 641–657. doi:10.1016/S0008-6223(01)00195-6.

[3] G. Savage, Carbon-carbon composites, Chapman and Hall, London, 1993. doi:10.1007/978-94-011-1586-5.

[4] E. Fitzer, L. M. Manocha, Carbon reinforcements and C/C composites, 1st ed., Berlin: Springer, 1998. doi:10.1007/978-3-642-58745-0.

[5] R. R. Naslain, The design of the fibre-matrix interfacial zone in ceramic matrix composites, Compos. Part A 29 (9) (1998) 1145–1155. doi:10.1016/S1359-835X(97)00128-0.

[6] R. R. Naslain, Design, preparation and properties of non-oxide CMCs for application in engines and nuclear reactors: an overview, Compos. Sci. Technol. 64 (2004) 155–170. doi:10.1016/S0266-3538(03)00230-6.

[7] E. Buet, J. Braun, C. Sauder, Influence of texture and thickness of pyrocarbon coatings as interphase on the mechanical behavior of specific 2.5D SiC/SiC composites reinforced with Hi-Nicalon S fibers, Coatings 12 (5) (2022). doi:10.3390/coatings12050573.

[8] J. Choury, Carbon-carbon materials for nozzles of solid propellant rocket motors, in: Proceedings of the 12^{th} Propulsion Conference, 1976. doi:10.2514/6.1976-609.

[9] S. Awasthi, J. L. Wood, Carbon/Carbon Composite Materials for Aircraft Brakes, John Wiley & Sons, Ltd, 1988, Ch. 4, pp. 553–559. doi:10.1002/9780470310496.ch4.

[10] H. Hatta, R. Weiß, P. David, Carbon/carbons and their industrial applications, in: N. P. Bansal, J. Lamon (Eds.), Ceramic Matrix Composites : Materials, Modeling and Technology, John Wiley & Sons, Ltd, 2014, Ch. 5, pp. 85–146. doi:10.1002/9781118832998.ch5.

[11] G. L. Vignoles, J. Lachaud, Y. Aspa, Environmental effects: Ablation of C/C materials – surface dynamics and effective reactivity, in: N. P. Bansal, J. Lamon (Eds.), Ceramic Matrix Composites: Materials, Modeling and Technology, Wiley & American Ceramic Society, 2014, Ch. 12, pp. 353–384. doi:10.1002/9781118832998.ch12.

[12] A. Wagner, M. Kuhn, J. M. Schramm, K. Hannemann, Experiments on passive hypersonic boundary layer control using ultrasonically absorptive carbon–carbon material with random microstructure, Exp. Fluids 54 (2013) 1606. doi:10.1007/s00348-013-1606-3.

[13] K. Swaminathan Gopalan, A. Borner, J. C. Ferguson, F. Panerai, N. N. Mansour, K. A. Stephani, Gas–surface interactions in lightweight fibrous carbon materials, Comput. Mater. Sci. 205 (2022) 111190. doi:10.1016/j.commatsci.2022.111190.

[14] T. S. Gross, K. Nguyen, M. Buck, N. Timoshchuk, I. I. Tsukrov, B. Reznik, R. Piat, T. Böhlke, Tension-compression anisotropy of in-plane elastic modulus for pyrolytic carbon, Carbon 49 (6) (2011) 2145 – 7. doi:10.1016/j.carbon.2011.01.012.

[15] J.-M. Gebert, B. Reznik, R. Piat, B. Viering, K. Weidenmann, A. Wanner, O. Deutschmann, Elastic constants of high-texture pyrolytic carbon measured by ultrasound phase spectroscopy, Carbon 48 (12) (2010) 3647–3650. doi:10.1016/j.carbon.2010.06.002.

[16] C. Sauder, J. Lamon, R. Pailler, The tensile properties of carbon matrices at temperatures up to 2200°c, Carbon 43 (10) (2005) 2054–2065. doi:10.1016/j.carbon.2005.03.020.

[17] G. Dong, K. Hüttinger, Consideration of reaction mechanisms leading to pyrolytic carbon of different textures, Carbon 40 (14) (2002) 2515–2528. doi:10.1016/S0008-6223(02)00174-4.

[18] V. De Pauw, B. Reznik, S. Kalhöfer, D. Gerthsen, Z. J. Hu, K. J. Hüttinger, Texture and nanostructure of pyrocarbon layers deposited on planar substrates in a hot-wall reactor, Carbon 41 (1) (2003) 71–7. doi:10.1016/S0008-6223(02)00272-5.

[19] H. Le Poche, X. Bourrat, M.-A. Dourges, G. L. Vignoles, F. Langlais, Influence of the gas-phase maturation on the CVD/CVI process and the micro-texture of laminar pyrocarbon from propane, in: M. Singh, R. J. Kerans, E. Lara-Curzio, R. Naslain (Eds.), Proceedings of the 5th intl. conf. on High-Temperature Ceramic Matrix Composites, The American Ceramic Society , Wiley, New York (NY, USA), 2005, pp. 293–300.

[20] M. Lieberman, H. Pierson, Effect of gas phase conditions on resultant matrix pyrocarbons in carbon/carbon composites, Carbon 12 (3) (1974) 233–241. doi:10.1016/0008-6223(74)90065-7.

[21] R. J. Diefendorf, W. E. Tokarsky, The relationships of structure to properties in graphite fibers, US Air Force report, AFML-TR-72-133 (1972).
URL https://apps.dtic.mil/sti/tr/pdf/AD0760573.pdf

[22] P. Dupel, X. Bourrat, R. Pailler, Structure of pyrocarbon infiltrated by pulse-CVI, Carbon 33 (9) (1995) 1193–1204. doi:10.1016/0008-6223(95)00029-D.

[23] X. Bourrat, B. Trouvat, G. Limousin, G. Vignoles, F. Doux, Pyrocarbon anisotropy as measured by electron diffraction and polarized light, J. Mater. Res. 15 (1) (2000) 92–101. doi:10.1557/JMR.2000.0017.

[24] B. Reznik, K. Hüttinger, On the terminology for pyrolytic carbon, Carbon 40 (4) (2002) 621–624. doi:10.1016/S0008-6223(01)00282-2.

[25] P. Weisbecker, J.-M. Leyssale, H. E. Fischer, V. Honkimäki, M. Lalanne, G. L. Vignoles, Microstructure of pyrocarbons from pair distribution function analysis using neutron diffraction, Carbon 50 (2012) 1563–1573. doi:10.1016/j.carbon.2011.11.035.

[26] B. Farbos, P. Weisbecker, H. Fischer, J.-P. Da Costa, M. Lalanne, G. Chollon, C. Germain, G. Vignoles, J.-M. Leyssale, Nanoscale structure and texture of highly anisotropic pyrocarbons revisited with transmission electron microscopy, image processing, neutron diffraction and atomistic modeling, Carbon 80 (2014) 472–489. doi:10.1016/j.carbon.2014.08.087.

[27] J.-M. Leyssale, J.-P. Da Costa, C. Germain, P. Weisbecker, G. L. Vignoles, Structural features of pyrocarbon atomistic models constructed from transmission electron microscopy images, Carbon 50 (12) (2012) 4388–4400. doi:10.1016/j.carbon.2012.05.015.

[28] B. Farbos, J.-P. Da Costa, G. Vignoles, J.-M. Leyssale, Nanoscale elasticity of highly anisotropic pyrocarbons, Carbon 94 (2015) 285–294. doi:10.1016/j.carbon.2015.06.060.

[29] A. P. Gillard, G. Couégnat, O. Caty, A. Allemand, P. Weisbecker, G. L. Vignoles, A quantitative, space-resolved method for optical anisotropy estimation in bulk carbons, Carbon 91 (2015) 423–435. doi:10.1016/j.carbon.2015.05.005.

[30] A. P. Gillard, G. Couégnat, S. Chupin, G. L. Vignoles, Modeling of the non-linear mechanical and thermomechanical behavior of 3d carbon/carbon composites based on internal interfaces, Carbon 154 (2019) 178–191. doi:10.1016/j.carbon.2019.07.101.

[31] J.-M. Leyssale, G. Couégnat, S. Jouannigot, G. L. Vignoles, Mechanisms of elastic softening in highly anisotropic carbons under in-plane compression/indentation, Carbon 197 (2022) 425–434. doi:10.1016/j.carbon.2022.06.063.

[32] F. Polewczyk, P. Lafourcade, J.-P. D. Costa, G. Vignoles, J.-M. Leyssale, Polygranular image guided atomistic reconstruction: A parametric model of pyrocarbon nanostructure, Carbon 212 (2023) 118109. doi:10.1016/j.carbon.2023.118109.

[33] F. Polewczyk, J.-M. Leyssale, P. Aurel, N. Pineau, C. Denoual, G. L. Vignoles, P. Lafourcade, Elasticity of dense anisotropic carbons: A machine learning model of the structure–property relationship informed by large scale molecular dynamics data, Acta Materialia (2024) 119851doi:10.1016/j.actamat.2024.119851.

[34] F. Polewczyk, J.-M. Leyssale, P. Lafourcade, Temperature-dependent elasticity of single crystalline graphite, Comput. Mater. Sci. 220 (2023) 112045. doi:10.1016/j.commatsci.2023.112045.

[35] X. Bourrat, A. Fillion, R. Naslain, G. Chollon, M. Brendlé, Regenerative laminar pyrocarbon, Carbon 40 (15) (2002) 2391–45. doi:10.1016/S0008-6223(02)00230-0.

[36] B. Farbos, H. Freeman, T. Hardcastle, J.-P. Da Costa, R. Brydson, A. J. Scott, P. Weisbecker, C. Germain, G. L. Vignoles, J.-M. Leyssale, A time-dependent atomistic reconstruction of severe irradiation damage and associated property changes in nuclear graphite, Carbon 120 (2017) 111–120. doi:10.1016/j.carbon.2017.05.009.

[37] F. Vuković, J.-M. Leyssale, P. Aurel, N. A. Marks, Evolution of threshold displacement energy in irradiated graphite, Phys. Rev. Appl. 10 (2018) 064040. doi:10.1103/PhysRevApplied.10.064040.

[38] J. W. Martin, J. L. Fogg, G. R. Francas, K. J. Putman, E. P. Turner, I. Suarez-Martinez, N. A. Marks, Graphite rapidly forms via annihilation of screw dislocations, Carbon 215 (2023) 118386. doi:10.1016/j.carbon.2023.118386.

[39] G. R. Francas, J. W. Martin, I. Suarez-Martinez, N. A. Marks, Topological defects and anisotropic development during pregraphitization, Carbon 213 (2023) 118251. doi:10.1016/j.carbon.2023.118251.

[40] S. I. Ranganathan, M. Ostoja-Starzewski, Universal elastic anisotropy index, Phys. Rev. Lett. 101 (2008) 055504. doi:10.1103/PhysRevLett.101.055504.

[41] L. Soulard, Molecular Dynamics Study of the Micro-spallation, Eur. Phys. J. D 50 (3) (2008). doi:10.1140/epjd/

e2008-00212-2.

[42] J. H. Los, L. M. Ghiringhelli, E. J. Meijer, A. Fasolino, Improved long-range reactive bond-order potential for carbon. I. Construction, Phys. Rev. B 72 (2005) 214102. doi:10.1103/PhysRevB.72.214102.

[43] L. Verlet, Computer" experiments" on classical fluids. II. Equilibrium correlation functions, Phys. Rev. 165 (1) (1968) 201. doi:10.1103/PhysRev.159.98.

[44] D. Franzblau, Computation of ring statistics for network models of solids, Phys. Rev. B 44 (1991) 4925–4930. doi:10.1103/PhysRevB.44.4925.

[45] J. Barthel, Dr. Probe: A software for high-resolution STEM image simulation, Ultramicroscopy 193 (2018) 1–11. doi:10.1016/j.ultramic.2018.06.003.

[46] K. Kim, Z. Lee, B. D. Malone, K. T. Chan, B. Alemán, W. Regan, W. Gannett, M. F. Crommie, M. L. Cohen, A. Zettl, Multiply folded graphene, Phys. Rev. B 83 (2011) 245433. doi:10.1103/PhysRevB.83.245433.

[47] N. G. Chopra, L. X. Benedict, V. H. Crespi, M. L. Cohen, S. G. Louie, A. Zettl, Fully collapsed carbon nanotubes, Nature 377 (1995) 135–138. doi:10.1038/377135a0.

[48] J. G. McHugh, P. Mouratidis, A. Impellizzeri, K. Jolley, D. Erbahar, C. P. Ewels, Prismatic edge dislocations in graphite, Carbon 188 (2022) 401–419. doi:10.1016/j.carbon.2021.11.072.

[49] T. Tohei, A. Kuwabara, F. Oba, I. Tanaka, Debye temperature and stiffness of carbon and boron nitride polymorphs from first principles calculations, Phys. Rev. B 73 (2006) 064304. doi:10.1103/PhysRevB.73.064304.

[50] B. G. A. Brito, L. Cândido, G.-Q. Hai, F. M. Peeters, Quantum effects in a free-standing graphene lattice: Path-integral against classical monte carlo simulations, Phys. Rev. B 92 (2015) 195416. doi:10.1103/PhysRevB.92.195416.

[51] C. P. Herrero, R. Ramírez, Quantum effects in graphene monolayers: Path-integral simulations, J. Chem. Phys. 145 (22) (2016) 224701. doi:10.1063/1.4971453.